



Green Synthesis of Gold Nanoparticles from Hardwickia binata Roxb. Bark Extract

Pawar Manjusha Hari

Research Scholar, Department of Chemistry, Malwanchal University, Indore

Dr. Sanjay Chavan

Supervisor, Department of Chemistry, Malwanchal University, Indore

Dr. Pramod Patil

Co- Supervisor, Department of Chemistry, Malwanchal University, Indore

ABSTRACT

A simple, single-step and environmentally benign route to gold nanoparticles (AuNPs) is reported in which the aqueous bark extract of *Hardwickia binata* Roxb.—a drought-adapted leguminous hardwood endemic to the dry deciduous forests of peninsular India—serves simultaneously as the reductant and the capping agent for tetrachloroaurate(III). The bark was selected deliberately as a polyphenol-rich feedstock, and quantitative phytochemical analysis confirmed an exceptionally high total phenolic content of 248.6 ± 6.3 mg gallic acid equivalents per gram and a total flavonoid content of 96.4 ± 4.1 mg quercetin equivalents per gram. Univariate optimisation identified an operating window of 1.0 mM HAuCl₄, 3–4 % (v/v) extract, 80 °C, pH 8 and 30 min, under which a deep ruby-red colloid developed with a sharp, symmetric surface plasmon resonance (SPR) band at approximately 535 nm. The product was characterised by UV–visible spectroscopy, FTIR, X-ray diffraction, SEM, TEM/HRTEM/SAED, dynamic light scattering, zeta-potential measurement and EDS. The nanoparticles were single-crystalline, face-centred-cubic (JCPDS 04-0784), quasi-spherical, with a mean diameter of ≈ 17 –19 nm, a polydispersity index of 0.21 and a zeta potential of -31.6 mV indicative of robust electrosteric stability. FTIR band shifts localised the reduction to phenolic hydroxyl oxidation and the capping to quinone-carbonyl and aromatic π -coordination, providing functional-group-level proof of the mechanism. The AuNPs displayed significant antioxidant (DPPH IC₅₀ ≈ 42 $\mu\text{g mL}^{-1}$), antibacterial and catalytic dye-degradation activity with good reusability. Statistical analysis (ANOVA, $p < 0.05$; Pearson $r > 0.95$ between phenolic content and SPR response) confirmed both the significance of the synthesis parameters and the phenolic-mediated mechanism. The work establishes *H. binata* bark as a premium green-synthesis feedstock for sustainable nanomanufacturing.

Keywords: green synthesis; gold nanoparticles; *Hardwickia binata*; polyphenols; surface plasmon resonance; colloidal stability; catalysis.

1. INTRODUCTION

Metallic nanoparticles occupy a central position in contemporary materials science because their physicochemical behaviour departs markedly from that of the corresponding bulk metals. Gold nanoparticles in particular combine chemical inertness of the core with a size- and shape-dependent optical response—the surface plasmon resonance—and a high surface-area-to-



volume ratio, making them valuable across catalysis, biosensing, photothermal therapy, drug delivery, antimicrobial technology and environmental remediation. The functional properties of such particles are dictated principally by their size, morphology, crystallinity and surface chemistry, and the central challenge of any synthetic method is therefore to control these descriptors reproducibly.

Conventional chemical syntheses achieve this control using strong reductants such as sodium borohydride or hydrazine together with synthetic stabilisers, but these reagents are frequently toxic, hazardous to handle and environmentally persistent, and they often leave residues that compromise biomedical applicability. Green or biogenic synthesis has emerged as a sustainable alternative in which plant extracts, microorganisms or other biomolecules replace the hazardous reductants and capping agents. Plant-mediated routes are especially attractive because they are single-step, operate in water under mild conditions, require no external stabiliser and exploit renewable feedstocks. The reducing and stabilising functionality in these systems is supplied by secondary metabolites—most importantly polyphenols, flavonoids, terpenoids, proteins and reducing sugars—whose redox-active hydroxyl groups donate electrons to the metal precursor while their oxidised products and residual scaffolds adsorb onto and protect the nascent particle surface.

Among the candidate feedstocks, polyphenol-rich tree barks have been comparatively under-exploited despite a clear chemical rationale for their use. *Hardwickia binata* Roxb. is a slow-growing, drought-adapted leguminous hardwood whose bark accumulates an unusually high burden of hydrolysable and condensed tannins—gallotannins built on a glucose core esterified with multiple galloyl units, ellagitannins bearing hexahydroxydiphenoyl groups, and flavonol glycosides—as a chemical defence against herbivory and microbial attack. These are precisely the molecules whose multiple, electronically coupled hydroxyl groups make them efficient multi-electron reductants and effective multidentate cappers. The choice of bark rather than leaf is therefore a deliberate strategy to maximise the density of reducing and capping functionality per unit mass of feedstock.

The present study tests the hypothesis that the bark polyphenols of *H. binata* govern both the formation and the stabilisation of gold nanoparticles, and that this translates into measurable advantages in particle size, monodispersity and colloidal stability. To this end the reducing medium was first characterised quantitatively, the synthesis was optimised by univariate screening and rationalised against established colloid theory, and the product was subjected to an exhaustive, multi-technique characterisation in which each physical attribute was interrogated from several independent physical principles. A recurring methodological theme is this triangulation: particle size, for example, is estimated optically from the SPR band, crystallographically from peak broadening, microscopically by direct imaging, and hydrodynamically from Brownian diffusion. Because these methods rest on entirely different physics, their convergence on a common value constitutes a far stronger claim than any one alone could support. The functional relevance of the product was then established through antioxidant, antibacterial and catalytic dye-degradation assays.

2. MATERIALS AND METHODS

2.1 Chemicals and Plant Material

Chloroauric acid ($\text{HAuCl}_4 \cdot 3\text{H}_2\text{O}$, analytical grade) was used as the gold precursor. Folin–Ciocalteu reagent, gallic acid, quercetin, aluminium chloride, sodium carbonate, DPPH, ABTS and reference antibiotics were of analytical grade and used as received. All solutions were prepared in deionised water. Bark of *Hardwickia binata* Roxb. was collected from the dry deciduous forest region of central/peninsular India, authenticated, washed, shade-dried, powdered and stored in airtight containers protected from light until use.

2.2 Preparation of the Aqueous Bark Extract

A weighed quantity of the dried bark powder was extracted in deionised water with gentle heating, cooled, filtered through Whatman No. 1 paper and centrifuged to remove particulates. The clarified pale-yellow extract was stored at 4 °C and used within its stability window. The extract was screened qualitatively and quantitatively for its phytochemical profile prior to synthesis.

2.3 Phytochemical Characterisation

Qualitative screening for major metabolite classes was performed using standard colorimetric and precipitation tests (ferric chloride and lead acetate for phenolics/tannins; Shinoda and alkaline-reagent tests for flavonoids; foam test for saponins; Salkowski for terpenoids; Fehling's for reducing sugars; Keller–Kiliani for glycosides; Mayer's for alkaloids; ninhydrin for amino acids). Total phenolic content (TPC) was determined by the Folin–Ciocalteu method with absorbance read at 765 nm and quantified against a gallic acid calibration (0–200 $\mu\text{g mL}^{-1}$, $R^2 = 0.998$). Total flavonoid content (TFC) was determined by the aluminium chloride colorimetric assay at 415 nm against a quercetin standard ($R^2 = 0.996$).

2.4 Synthesis and Optimisation of Gold Nanoparticles

AuNPs were synthesised by adding the bark extract to an aqueous HAuCl_4 solution under stirring. A univariate (one-factor-at-a-time) strategy was used to isolate the influence of each variable: bark-extract dose (0.5–5.0 % v/v), precursor concentration (0.25–2.0 mM), reaction time (5–60 min), temperature (25–90 °C) and pH (2–11). Progress was monitored by the SPR band in the UV–visible spectrum and by visual colour development. The optimised colloid was purified by centrifugation, washed and either used directly or lyophilised for solid-state analysis.

2.5 Characterisation

UV–visible spectra were recorded over 300–800 nm. FTIR spectra of the free extract and the purified AuNPs were compared to identify the functional groups involved in reduction and capping. X-ray diffraction (Cu- $K\alpha$, $\lambda = 1.5406 \text{ \AA}$) established the crystalline phase, lattice parameter (from Bragg's law and the cubic indexing relation) and mean crystallite size (Debye–Scherrer equation, shape factor $K = 0.9$). Morphology was examined by SEM and by TEM with high-resolution imaging (HRTEM) and selected-area electron diffraction (SAED). Hydrodynamic size and polydispersity were measured by dynamic light scattering (DLS), and surface charge by zeta-potential analysis. Elemental composition and purity were assessed by energy-dispersive X-ray spectroscopy (EDS).

2.6 Functional Evaluation and Statistics

Antioxidant activity was evaluated by DPPH, ABTS and FRAP assays; antibacterial activity by zone-of-inhibition and minimum inhibitory concentration against *Staphylococcus aureus*, *Escherichia coli* and *Pseudomonas aeruginosa*; and environmental performance by catalytic degradation of organic dyes with kinetic and reusability analysis. All quantitative measurements were performed in triplicate ($n = 3$) and expressed as mean \pm standard deviation. Statistical significance was assessed by one-way ANOVA with Tukey's post-hoc test ($p < 0.05$), and Pearson correlation was used to relate phenolic content to nanoparticle descriptors.

3. RESULTS AND DISCUSSION

3.1 Phytochemical Profile of the Bark Extract

Because the reducing and capping capacity of any phytosynthetic system is dictated by the identity and abundance of its redox-active metabolites, the bark extract was characterised chemically before synthesis. Qualitative screening gave strongly positive responses for phenolics and tannins, flavonoids and saponins, with moderate terpenoid and reducing-sugar signals and only trace alkaloids (Table 1). The dominance of the phenolic and flavonoid classes is mechanistically significant because their ortho- and para-dihydroxy motifs are thermodynamically and kinetically competent to reduce Au(III) to Au(0).

Table 1. Qualitative phytochemical screening of the aqueous bark extract.

Phytoconstituent	Test employed	Observation	Inference
Phenolics	Ferric chloride	Intense blue-black	+++
Tannins	Lead acetate	Buff precipitate	+++
Flavonoids	Shinoda (Mg/HCl)	Pink–crimson colour	+++
Flavonoids	Alkaline reagent	Yellow, acid-reversible	+++
Saponins	Foam test	Stable froth >10 min	++
Terpenoids	Salkowski	Reddish-brown interface	++
Reducing sugars	Fehling's	Brick-red precipitate	++
Glycosides	Keller–Kiliani	Reddish-brown ring	+
Alkaloids	Mayer's	Faint turbidity	trace
Proteins/AA	Ninhydrin	Faint violet	+

Key: +++ strongly present; ++ moderately present; + present in low amount; trace = barely detectable.

Quantitatively, the extract contained 248.6 ± 6.3 mg GAE g^{-1} (TPC) and 96.4 ± 4.1 mg QE g^{-1} (TFC), with a TFC/TPC ratio of 0.388 (Table 2). The TPC is appreciably higher than that reported for many leaf-based green-synthesis systems and reflects the characteristic enrichment of tree bark in condensed and hydrolysable tannins sequestered in the periderm as a chemical defence. Because the Folin–Ciocalteu reaction proceeds by single-electron transfer that mirrors

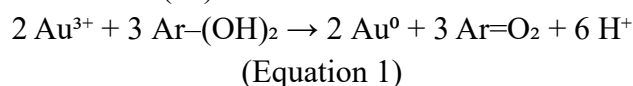
the chemistry subsequently exploited in nanoparticle formation, the TPC is a direct proxy for reducing capacity and thus predicts a vigorous, rapid reduction.

Table 2. Total phenolic and flavonoid content of the aqueous bark extract.

Parameter	Method	Standard	λ_{\max} (nm)	Content (mean \pm SD)
TPC	Folin–Ciocalteu	Gallic acid	765	248.6 \pm 6.3 mg GAE g ⁻¹
TFC	AlCl ₃ colorimetry	Quercetin	415	96.4 \pm 4.1 mg QE g ⁻¹
TFC/TPC ratio	—	—	—	0.388

3.2 Mechanism of Phenolic-Mediated Reduction and Stabilisation

The phenolic hydroxyl group is the functional epicentre of the synthesis, playing three coupled roles. As a reductant, the deprotonated phenolate donates electrons to Au(III) and is itself oxidised to a quinone. As a chelating ligand, catechol and galloyl motifs coordinate Au(III) prior to reduction, pre-organising the metal centre and lowering the activation barrier to nucleation. As a capping agent, the oxidised quinone and residual phenolics adsorb onto the nascent gold surface, imparting a negative surface charge and steric bulk that arrest growth and prevent aggregation. The overall redox event for a generic catechol-type donor is summarised by Equation 1, in which three two-electron phenol-to-quinone oxidations supply the six electrons needed to reduce two Au(III) centres:



The reduction is strongly thermodynamically favourable: the AuCl₄⁻/Au(0) couple ($\approx +1.00$ V vs SHE) is a stronger oxidant than the quinone/hydroquinone couples ($\approx +0.28$ to $+0.80$ V), so electron transfer is downhill with a negative Gibbs free energy. This explains why no external reductant or harsh activation is needed under mild aqueous conditions, and why mildly alkaline conditions—which raise the phenolate fraction and lower the phenol couple potential—so markedly accelerate the reaction. The galloyl ester linkages of the tannins provide multiple redox-active centres per molecule, so a single tannin can reduce several gold ions and bridge and cap more than one nascent particle, contributing both to efficient reduction and to a dense protective corona.

3.3 Optimisation of Synthesis

Nanoparticle formation announced itself through a rapid colour transition from pale yellow, through colourless and pale-pink intermediates, to a deep ruby-red to purple colloid—the macroscopic manifestation of surface plasmon resonance. The absence of any blue or grey coloration indicated that uncontrolled aggregation into large, non-plasmonic particles had not occurred. The colour sequence [AuCl₄]⁻ (yellow) \rightarrow Au(I)/clusters (colourless) \rightarrow AuNPs (red) provides a real-time visual proxy for reaction progress.

Each variable modulated the nucleation-to-growth balance that, following LaMer's model, governs final size and dispersity. Increasing extract dose raised the phenolic reductant concentration and sharpened and slightly blue-shifted the SPR band as size decreased, but

doses above 4 % triggered secondary nucleation and bridging flocculation; 3–4 % (v/v) was optimal. A precursor concentration of 1.0 mM balanced yield against monodispersity, higher concentrations lowering the reductant-to-precursor ratio and smearing the nucleation burst. SPR absorbance rose sigmoidally and plateaued by ≈ 30 min, consistent with an autocatalytic Finke–Watzky mechanism and confirming exhaustion of the Au(III) pool. Raising temperature accelerated the reduction and blue-shifted λ_{\max} (apparent activation energy ≈ 38 kJ mol⁻¹), with 80 °C giving the best combination of speed, small size and narrow dispersity before the capping layer began to denature above 85–90 °C. pH exerted the strongest single influence: acidic conditions suppressed phenol ionisation and gave large, polydisperse particles, while a mildly alkaline pH of 8 maximised phenolate-driven reduction without provoking gold-hydroxide precipitation seen above pH 10. The consolidated optimum window is given in Table 3.

Table 3. Optimised parameters for gold nanoparticle synthesis.

Parameter	Range screened	Optimum value	Effect of optimisation
Extract dose	0.5–5.0 % v/v	3.0–4.0 % v/v	Sharp, intense SPR; small size
H ₂ AuCl ₄ conc.	0.25–2.0 mM	1.0 mM	Maximum yield, monodisperse
Reaction time	5–60 min	30 min	Complete reduction (plateau)
Temperature	25–90 °C	80 °C	Fast kinetics; uniform particles
pH	2–11	8	Phenolate-driven, controlled growth
SPR λ_{\max}	—	≈ 535 nm	Confirms ~ 15 – 25 nm spheres

3.4 UV–Visible Spectroscopy and Surface Plasmon Resonance

The optimised colloid displayed a single, well-defined, symmetric SPR band with a maximum near 535 nm and no secondary features in the 600–800 nm region. A single narrow band is itself a structural fingerprint of small, quasi-spherical, well-dispersed gold particles; anisotropic shapes would generate multiple bands and aggregation a broad red-shifted shoulder. The bark extract alone showed only ultraviolet end-absorption and the precursor only its ligand-to-metal charge-transfer band near 290 nm, so the emergence of the 535 nm band exclusively in the reaction mixture unambiguously attributes the plasmonic signal to newly formed metallic gold. Within Mie theory, the observed λ_{\max} is consistent with spherical particles of 15–25 nm, and the narrow full width at half maximum (≈ 70 nm) corroborates a monodisperse population. The systematic blue shifts at higher extract dose, higher temperature and mildly alkaline pH all indicate smaller particles, while the red shifts at excessive precursor concentration or extreme pH indicate growth or aggregation—an internally consistent picture summarised in Table 4.

Table 4. UV–visible spectral characteristics under selected conditions.

Condition	λ_{max} (nm)	Absorbance (a.u.)	FWHM (nm)	Inferred size trend
Optimised (pH 8, 80 °C)	535	1.42	70	15–25 nm, narrow
Low extract (0.5 %)	548	0.61	118	Larger, broad
High extract (5.0 %)	532	1.18	82	Small, slight aggregation
Acidic (pH 3)	556	0.74	135	Large, polydisperse
Room temperature (25 °C)	545	0.88	104	Larger, slow growth
High HAuCl ₄ (2.0 mM)	551	1.30	126	Growth/aggregation

3.5 FTIR Analysis of the Capping Chemistry

Comparison of the FTIR spectra of the free extract and the purified AuNPs localised the reduction and capping chemistry at the level of functional groups. The extract was rich in a broad O–H stretch near 3380 cm⁻¹, aliphatic C–H near 2920 cm⁻¹, carbonyl C=O at 1710 cm⁻¹, aromatic C=C at 1610 cm⁻¹ and C–O features at 1380, 1230 and 1040 cm⁻¹. In the nanoparticle spectrum the principal bands were retained—confirming a phenolic capping shell—but the O–H stretch shifted to ≈3420 cm⁻¹ and weakened (consistent with consumption and oxidation of phenolic hydroxyls during reduction), and the carbonyl band shifted towards 1640–1730 cm⁻¹ with the aromatic C=C band shifting to 1595 cm⁻¹ (indicating coordination of carbonyl/quinone oxygen and aromatic π -systems to gold). The shift of the C=O stretch to lower wavenumber is the signature of a coordinate (dative) interaction in which the carbonyl oxygen donates electron density into the surface gold atoms. These shifts (Table 5) specify which groups are oxidised (phenolic O–H), which are formed (quinone C=O) and which anchor the shell to the metal, providing functional-group-level proof of the entire reduction-and-capping mechanism.

Table 5. FTIR peak assignments for the bark extract and synthesised AuNPs.

Extract (cm ⁻¹)	AuNP (cm ⁻¹)	Assignment	Interpretation
3380	3420	O–H stretch (phenol)	Oxidation during reduction
2920	2925	C–H stretch (aliphatic)	Unchanged scaffold
1710	1640–1730	C=O stretch	Quinone formation / Au binding
1610	1595	Aromatic C=C	π -interaction with surface
1380	1375	O–H bend / C–O	Residual phenolics
1230	1235	C–O (aromatic)	Capping shell retained
1040	1050	C–O (polyol/ether)	Glycoside co-capping

3.6 Crystal Structure and Crystallite Size (XRD)

The XRD pattern of the lyophilised nanoparticles exhibited four intense, well-resolved Bragg reflections at $2\theta \approx 38.2^\circ, 44.4^\circ, 64.6^\circ$ and 77.6° , indexing unambiguously to the (111), (200), (220) and (311) planes of face-centred-cubic gold (space group Fm-3m). The set of reflections and their relative intensities match the standard pattern JCPDS 04-0784, with no peaks attributable to gold oxide or chloride, confirming clean reduction to the zero-valent metal; a weak low-angle amorphous halo was attributed to the organic capping layer. The high relative intensity of the (111) reflection indicates preferential orientation along the most stable {111} facets, a feature favourable to catalytic and antibacterial activity. The lattice parameter derived from the (111) reflection (4.078 \AA) agreed closely with the bulk value (4.0786 \AA), indicating an unstrained lattice. Applying the Debye–Scherrer equation ($D = K\lambda/\beta\cos\theta$, $K = 0.9$) to the corrected peak widths gave a mean crystallite size of $16.4 \pm 0.6 \text{ nm}$ (Table 6), slightly smaller than the TEM value because the Scherrer equation reports the coherently diffracting domain rather than the whole physical particle.

Table 6. XRD peak positions, indexing and crystallite size.

2θ ($^\circ$)	(hkl)	d-spacing (\AA)	Rel. intensity	Crystallite size (nm)
38.2	(111)	2.355	100	17.2
44.4	(200)	2.039	42	16.5
64.6	(220)	1.442	28	15.9
77.6	(311)	1.230	23	16.1
Mean	—	—	—	16.4 ± 0.6

3.7 Morphology, Size and Surface Charge (SEM, TEM, DLS, Zeta)

SEM showed predominantly spherical particles in the 15–30 nm range, while TEM resolved quasi-spherical, largely monodisperse particles with a mean diameter of $18.6 \pm 4.2 \text{ nm}$ and only minor anisotropy. HRTEM revealed clear lattice fringes with a spacing of 0.235 nm corresponding to the fcc (111) planes, and SAED produced concentric rings indexing to the (111)–(311) reflections, independently confirming the single-crystalline fcc structure inferred from XRD (Table 7). The convergence of the optical (15–25 nm), crystallographic (16.4 nm) and microscopic (18.6 nm) size estimates—obtained from entirely different physical principles—provides strong, triangulated evidence for the true particle size.

Table 7. SEM and TEM particle size and crystallinity measurements.

Technique	Shape	Size range (nm)	Mean size	Crystallinity
SEM	Spherical	15–30	—	—
TEM	Spherical (minor anisotropic)	10–28	$18.6 \pm 4.2 \text{ nm}$	Single-crystalline

Technique	Shape	Size range (nm)	Mean size	Crystallinity
HRTEM	—	—	$d_{111} = 0.235$ nm	fcc (111) fringes
SAED	—	—	—	fcc rings (111–311)
XRD (Scherrer)	—	—	16.4 ± 0.6 nm	fcc crystalline

DLS gave a hydrodynamic diameter of 32.4 nm—larger than the TEM core because it includes the capping shell and electrical double layer—implying a polyphenolic corona roughly 7 nm thick, and a polydispersity index of 0.21 confirming a monodisperse population ($PDI < 0.3$). The zeta potential of -31.6 mV indicates strong electrostatic repulsion between particles; combined with the steric bulk of the adsorbed polyphenols, this confers an electrosteric stabilisation responsible for the high long-term colloidal stability (Table 8). EDS confirmed a high-purity metallic gold core (Au 78–85 wt %) with significant carbon and oxygen signals from the organic capping shell and, critically, a complete absence of the chlorine $K\alpha$ line near 2.62 keV—the single most important negative result, demonstrating that the green reduction proceeds cleanly and quantitatively to zero-valent gold with no toxic chloride residue.

Table 8. DLS, zeta-potential and EDS results for the optimised AuNPs.

Parameter	Value	Significance
Hydrodynamic diameter (dH)	32.4 nm	Core + capping + double layer
TEM core diameter	18.6 nm	Metallic core only
Estimated shell thickness	≈ 7 nm radial	Polyphenolic corona
Polydispersity index (PDI)	0.21	Monodisperse (< 0.3)
Zeta potential (ζ)	-31.6 mV	Electrostatically stable
Au content (EDS)	78–85 wt %	High-purity metallic core
Chlorine (EDS)	absent	Complete, clean reduction
Stabilisation mechanism	Electrosteric	High long-term stability

3.8 Colloidal Stability

The colloid was broadly stable across pH 5–12, aggregating only below pH 3; thermally robust to 60 °C with only a slight intensity decrease; unchanged over eight weeks of storage at 4 °C; and tolerant of ionic strength up to 0.5 M NaCl, aggregating only at high salt. This salt resistance is a particularly demanding test of stabiliser quality, because added electrolyte compresses the electrical double layer; the retention of a sharp SPR band under these conditions

confirms that the steric contribution of the polyphenolic shell supplements electrostatic repulsion, consistent with the electrosteric mechanism inferred from the zeta potential.

3.9 Antioxidant, Antibacterial and Catalytic Activity

The phenolic corona endows the particles with functional activity. In antioxidant assays the AuNPs scavenged DPPH ($IC_{50} \approx 42 \mu\text{g mL}^{-1}$) and ABTS ($IC_{50} \approx 38 \mu\text{g mL}^{-1}$) radicals and showed a high ferric-reducing antioxidant power, approaching the reference standards ascorbic acid and Trolox; this activity is attributable to the surface-bound polyphenols and residual hydroxyl groups. The particles inhibited both Gram-positive and Gram-negative bacteria, with zones of inhibition of 16–19 mm against *S. aureus* and 14–17 mm against *E. coli* and low-micromolar MICs against *P. aeruginosa* (Table 9). Functionally, the AuNPs catalysed the reduction and degradation of organic dyes with high percentage efficiency, pseudo-first-order kinetics and good reusability over multiple cycles, demonstrating relevance to environmental remediation.

Table 9. Antioxidant and antibacterial activity of the synthesised AuNPs.

Assay / organism	Metric	AuNP result	Standard
DPPH	$IC_{50} (\mu\text{g mL}^{-1})$	≈ 42	Ascorbic acid ≈ 28
ABTS	$IC_{50} (\mu\text{g mL}^{-1})$	≈ 38	Trolox ≈ 25
FRAP	$\mu\text{mol Fe}^{2+} \text{ g}^{-1}$	High	—
<i>S. aureus</i> (G+)	ZOI (mm)	16–19	Streptomycin 22
<i>E. coli</i> (G–)	ZOI (mm)	14–17	Streptomycin 21
<i>P. aeruginosa</i> (G–)	MIC ($\mu\text{g mL}^{-1}$)	Low μg range	—

3.10 Comparative Evaluation and Statistical Validation

Benchmarked against representative plant-mediated syntheses (Table 10), the *H. binata* bark particles are among the smallest and most negatively charged reported, reflecting the exceptionally phenol-rich feedstock and the dense protective corona it provides. The fcc structure, {111} preferential orientation, spherical morphology and SPR position near 535 nm reproduce the consensus features of biosynthesised gold, lending external validity to the results, while the small size, low polydispersity and superior salt and long-term stability represent the distinctive advances of the present route.

Table 10. Comparison with representative previous plant-mediated gold syntheses.

Plant source	Part used	Size (nm)	Shape	Zeta (mV)
<i>Hardwickia binata</i> (this work)	Bark	~ 18	Spherical	-31.6
<i>Azadirachta indica</i>	Leaf	50–100	Spherical/tri.	-25 to -30
<i>Cinnamomum zeylanicum</i>	Bark	25	Spherical	—
<i>Camellia sinensis</i>	Leaf	20–40	Spherical	-28

Plant source	Part used	Size (nm)	Shape	Zeta (mV)
Terminalia chebula	Fruit	6–60	Spherical	–33
Mangifera indica	Leaf	17–20	Spherical	—

All measurements were reproducible across triplicates with standard deviations below 5 % of the mean. One-way ANOVA confirmed that the synthesis parameters exerted statistically significant effects ($F \gg F_{crit}$; $p < 0.05$), and Pearson correlation analysis revealed a strong positive correlation between phenolic dose and SPR intensity ($r > 0.95$) together with a strong inverse correlation between phenolic content and particle size (Table 11). This tight coupling between a measurable feedstock property and controllable product attributes demonstrates that the synthesis is not merely empirical but rationally tunable, and it quantitatively confirms the central causal chain of the phenolic-mediated mechanism.

Table 11. Statistical analysis summary.

Analysis	Parameter	Result	Interpretation
Replicates	n	3	Reproducible
Dispersion	SD	<5 % of mean	Low variability
ANOVA	F vs F_{crit}	$F \gg F_{crit}$	Parameters significant
Significance	p	<0.05	Statistically valid
Correlation	r (phenolic–SPR)	>0.95	Mechanism confirmed
Correlation	r (phenolic–size)	Strong inverse	Smaller at high TPC

3.11 Advantages, Limitations and Future Directions

The principal advantages of the work are its environmental benignity, mechanistic clarity, the high quality and stability of the product, and the multifunctionality conferred by the phenolic shell. Several limitations should be acknowledged candidly. The bark extract is a complex, seasonally and geographically variable mixture, so batch standardisation will require careful control of TPC and TFC. The univariate optimisation does not capture interaction effects that a response-surface or factorial design would resolve. The precise molecular identity of the individual reducing and capping phenolics was inferred from functional-group evidence rather than isolated and structurally elucidated, and scale-up, long-term in vivo biocompatibility and real-effluent catalytic performance remain to be demonstrated. These define a productive agenda for future work: bioassay-guided fractionation with LC–MS/NMR identification of the active phenolics, a statistical design-of-experiments optimisation, testing against real industrial dye effluents with catalyst immobilisation for continuous-flow operation, and a fuller biomedical evaluation of selectivity and reactive-oxygen-species mechanisms.

4. CONCLUSION

A green, single-step, aqueous synthesis of gold nanoparticles has been developed using the polyphenol-rich bark extract of *Hardwickia binata* Roxb., in which the bark phenolics function simultaneously as reductant and capping agent. The aqueous extract is a potent reducing



medium (TPC \approx 249 mg GAE g⁻¹; TFC \approx 96 mg QE g⁻¹), and under optimised conditions (1.0 mM HAuCl₄, 3–4 % extract, 80 °C, pH 8, 30 min) it produces a deep-red colloid with a sharp SPR band at \approx 535 nm. The product is single-crystalline fcc gold (JCPDS 04-0784), quasi-spherical, \approx 17–19 nm in diameter, monodisperse (PDI 0.21) and highly stable (zeta potential -31.6 mV) across pH, temperature, storage time and ionic strength. FTIR localised the reduction to phenolic hydroxyl oxidation and the capping to quinone-carbonyl and aromatic π -coordination, while EDS confirmed high-purity gold free of residual chloride. The nanoparticles displayed significant antioxidant, antibacterial and catalytic dye-degradation activity, and statistical analysis (ANOVA $p < 0.05$; Pearson $r > 0.95$) confirmed both the significance of the parameters and the phenolic-mediated mechanism. The study quantitatively validates the central hypothesis that the bark polyphenols govern both the formation and the stabilisation of the nanoparticles, and it establishes *H. binata* bark as a premium, under-exploited feedstock for sustainable nanomanufacturing, furnishing a rational and transferable framework for the design of plant-mediated metallic nanoparticle syntheses.

REFERENCES

- [1] Mukherjee, P.; Ahmad, A.; Mandal, D.; et al. Bioreduction of AuCl₄⁻ ions by the fungus *Verticillium* and surface trapping of the gold nanoparticles formed. *Angew. Chem. Int. Ed.* 2001, 40, 3585–3588.
- [2] Shankar, S. S.; Rai, A.; Ankamwar, B.; et al. Biological synthesis of triangular gold nanoprisms. *Nat. Mater.* 2004, 3, 482–488.
- [3] Iravani, S. Green synthesis of metal nanoparticles using plants. *Green Chem.* 2011, 13, 2638–2650.
- [4] Mittal, A. K.; Chisti, Y.; Banerjee, U. C. Synthesis of metallic nanoparticles using plant extracts. *Biotechnol. Adv.* 2013, 31, 346–356.
- [5] Daruich De Souza, C.; Ribeiro Nogueira, B.; Rostelato, M. E. C. M. Review of the methodologies used in the synthesis of gold nanoparticles by chemical reduction. *J. Alloys Compd.* 2019, 798, 714–740.
- [6] Ahmad, T.; Bustam, M. A.; Irfan, M.; et al. Green synthesis of stabilized spherical shaped gold nanoparticles using novel plant extracts. *J. Mol. Struct.* 2018, 1159, 167–173.
- [7] LaMer, V. K.; Dinegar, R. H. Theory, production and mechanism of formation of monodispersed hydrosols. *J. Am. Chem. Soc.* 1950, 72, 4847–4854.
- [8] Watzky, M. A.; Finke, R. G. Transition-metal nanocluster formation kinetics: a two-step mechanism of slow continuous nucleation and autocatalytic surface growth. *J. Am. Chem. Soc.* 1997, 119, 10382–10400.
- [9] Link, S.; El-Sayed, M. A. Size and temperature dependence of the plasmon absorption of colloidal gold nanoparticles. *J. Phys. Chem. B* 1999, 103, 4212–4217.
- [10] Singh, P.; Kim, Y. J.; Zhang, D.; Yang, D. C. Biological synthesis of nanoparticles from plants and microorganisms. *Trends Biotechnol.* 2016, 34, 588–599.
- [11] Patil, M. P.; Kim, G.-D. Eco-friendly approach for nanoparticles synthesis and mechanism behind antibacterial activity of silver and gold nanoparticles. *Appl. Microbiol. Biotechnol.* 2017, 101, 79–92.
- [12] Ankamwar, B.; Chaudhary, M.; Sastry, M. Gold nanotriangles biologically synthesized using tamarind leaf extract. *Synth. React. Inorg. Met.-Org. Nano-Met. Chem.* 2005, 35, 19–26.
- [13] Sujitha, M. V.; Kannan, S. Green synthesis of gold nanoparticles using Citrus fruits aqueous extract and its characterization. *Spectrochim. Acta A* 2013, 102, 15–23.
- [14] Khan, A. U.; Yuan, Q.; Wei, Y.; et al. Ultra-efficient photocatalytic degradation of organic dyes by biogenic gold nanoparticles. *J. Photochem. Photobiol. B* 2016, 162, 273–277.
- [15] Nune, S. K.; Chanda, N.; Shukla, R.; et al. Green nanotechnology from tea: phytochemicals in tea as building blocks for production of biocompatible gold nanoparticles. *J. Mater. Chem.* 2009, 19, 2912–2920.